

CHMP2B mutants linked to frontotemporal dementia impair maturation of dendritic spines

Agnès Belly^{1,2}, Gilles Bodon^{1,2}, Béatrice Blot^{1,2}, Alexandre Bouron^{3,4,5}, Rémy Sadoul^{1,2} and Yves Goldberg^{1,2,3,*}

¹INSERM, Research Centre U836 and ²Université Joseph Fourier, Grenoble Institute of Neurosciences, Campus Santé, F-38042 Grenoble, France

³CEA, DSV, iRTSV, ⁴CNRS, UMR 5249 and ⁵Université Joseph Fourier, UMR 5249, F-38054 Grenoble, France

*Author for correspondence (yves.goldberg@ujf-grenoble.fr)

Accepted 27 May 2010

Journal of Cell Science 123, 2943–2954

© 2010. Published by The Company of Biologists Ltd

doi:10.1242/jcs.068817

Summary

The highly conserved ESCRT-III complex is responsible for deformation and cleavage of membranes during endosomal trafficking and other cellular activities. In humans, dominant mutations in the ESCRT-III subunit CHMP2B cause frontotemporal dementia (FTD). The decade-long process leading to this cortical degeneration is not well understood. One possibility is that, akin to other neurodegenerative diseases, the pathogenic protein affects the integrity of dendritic spines and synapses before any neuronal death. Using confocal microscopy and 3D reconstruction, we examined whether expressing the FTD-linked mutants CHMP2B^{intron5} and CHMP2B^{Δ10} in cultured hippocampal neurons modified the number or structure of spines. Both mutants induced a significant decrease in the proportion of large spines with mushroom morphology, without overt degeneration. Furthermore, CHMP2B^{Δ10} induced a drop in frequency and amplitude of spontaneous excitatory postsynaptic currents, suggesting that the more potent synapses were lost. These effects seemed unrelated to changes in autophagy. Depletion of endogenous CHMP2B by RNAi resulted in morphological changes similar to those induced by mutant CHMP2B, consistent with dominant-negative activity of pathogenic mutants. Thus, CHMP2B is required for spine growth. Taken together, these results demonstrate that a mutant ESCRT-III subunit linked to a human neurodegenerative disease can disrupt the normal pattern of spine development.

Key words: ESCRT, FTLD, Neurodegeneration, Synapse, Spine head, NeuronStudio

Introduction

The endosomal sorting complexes required for transport (ESCRT) are a set of four cytoplasmic protein complexes (ESCRT-0 to ESCRT-III), conserved from yeast to human. ESCRTs are central to a growing range of cellular activities, including the delivery of downregulated surface proteins to the lumen of late endosomes (Hurley and Emr, 2006; Slagsvold et al., 2006), the release of viruses at the plasma membrane (von Schwedler et al., 2003), cytokinesis of dividing cells (Carlton and Martin-Serrano, 2007) and autophagy of protein aggregates (Filimonenko et al., 2007). All of these diverse processes involve the budding and fission of cellular membranes, the latter of which seems to be directly catalysed by ESCRTs. Recent results show that ESCRTs are sequentially recruited to the cytosolic side of endosomal or plasma membrane microdomains, until ESCRT-III subunits locally polymerise into filaments. Transient assembly of ESCRT-III filaments on the membrane is a physical agent of membrane deformation and vesiculation (Fabrikant et al., 2009; Hanson et al., 2008; Lata et al., 2008; Muziol et al., 2006; Saxena et al., 2009; Wollert et al., 2009; Wollert and Hurley, 2010). Hence, ESCRT-III polymers are pivotal effectors of cellular membrane restructuring.

In keeping with its potent effects, the polymerisation of ESCRT-III is normally under tight regulation. The core subunits of ESCRT-III form a family of highly related proteins, the charged multivesicular body proteins (CHMP) 1–7, all of which contain a conserved oligomerisation and lipid-binding interface (the ESCRT-III or SNF-7 domain), linked to a C-terminal regulatory region (see Fig. 1). The latter mediates both intramolecular inhibition of the

ESCRT-III domain and intermolecular interaction with subunit-specific factors that regulate filament dynamics (Bajorek et al., 2009; Muziol et al., 2006; Stuchell-Brereton et al., 2007; Zamborlini et al., 2006). Deletion of the regulatory region converts ESCRT-III subunits into dominant-negative mutants that are able to block ESCRT-dependent processes such as the release of HIV-1 virions from infected cells (Zamborlini et al., 2006).

Among the ESCRT-III subunits, CHMP2B has received particular attention following the discovery that mutations in the *CHMP2B* gene underlie a dominantly heritable form of frontotemporal dementia (called FTD-3), a presenile brain disease caused by selective degeneration of cortical neurons (Skibinski et al., 2005). In a thoroughly studied Danish kindred, the FTD phenotype was tightly linked to a single point mutation at the splice acceptor site of *CHMP2B* exon 6. The mutation generates two distinct aberrant transcripts, *CHMP2B*^{intron5} and *CHMP2B*^{Δ10}, both of which encode proteins with a defective C terminus (Skibinski et al., 2005) (see Fig. 1). Neurodegeneration has been hypothesised to result from perturbation of neuronal autophagy by these mutant subunits (Rusten and Simonsen, 2008). Consistent with the loss of the regulatory domain, in heterologous cells, both CHMP2B^{intron5} and CHMP2B^{Δ10} form insoluble polymers, often coating endosomes, and cause dominant-negative inhibition of ESCRT-dependent processes, including autophagosome maturation (Filimonenko et al., 2007; Lee et al., 2007; Skibinski et al., 2005). In cultured cortical neurons, overexpression of CHMP2B^{intron5} was shown to induce retraction of dendritic arbors and subsequent cell death, partly through toxic build-up of autophagosomes (Lee et al.,

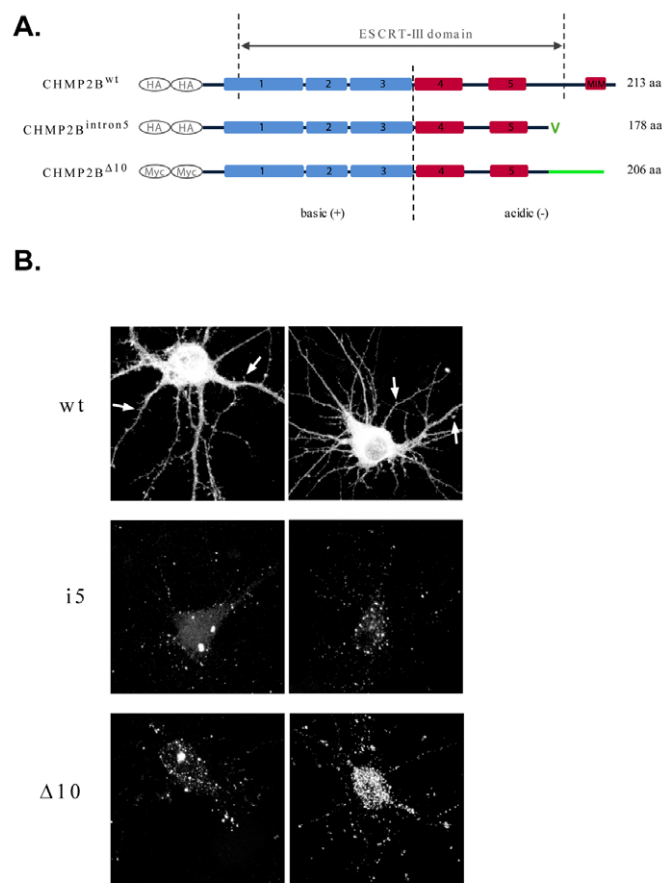


Fig. 1. Structure and distribution of CHMP2B constructs. (A) Primary structure of CHMP2B constructs used in this study. The ESCRT-III domain is the conserved sequence domain common to all members of the charged multivesicular body proteins (CHMP1–7) superfamily. Positively (blue) and negatively (red) charged α helices (1–5) are located along the sequence according to the 3D structure of the closely related CHMP3 protein (Muziol et al., 2006). MIM: microtubule interacting and transport domain (MIT)-interacting module, required for binding to the SKD1 (Vps4) ATPase responsible for dissociation of CHMP polymers. V: a single valine residue replaces the normal C-terminus in CHMP2B^{intron5}. The green line in CHMP2B^{Δ10} indicates the aberrant C-terminus carried by this mutant. Ellipses indicate tags fused to the N-terminus (tags are nine or ten residues long). Sequence lengths are those of the untagged proteins. (B) Subcellular distribution of tagged CHMP2B proteins. Neurons were transfected with the indicated plasmids, processed for immunofluorescence staining with anti-tag antibody and imaged by confocal microscopy. Two representative cells are shown for each plasmid. Top: CHMP2B^{wt} diffuses throughout the entire neuron, including the heads of dendritic spines (arrows). Middle: CHMP2B^{intron5} forms multiple small clusters in the soma and dendrites, and occasional larger aggregates. Bottom: CHMP2B^{Δ10} has a clustered distribution similar to that of CHMP2B^{intron5}.

2007; Lee and Gao, 2009). Surprisingly, however, CHMP2B^{Δ10} failed to increase neuronal death, even though its effects in heterologous cells on autophagy are similar to those of CHMP2B^{intron5} (Filimonenko et al., 2007). Furthermore, knockdown of CHMP2B by RNAi did not modify neuronal viability. These observations suggest that disease-linked CHMP2B mutations might affect neuronal physiology in ways other than by lethal malfunction of autophagic mechanisms.

Accumulating evidence indicates that, in various neurodegenerative diseases, neuronal death is a late event, preceded by early disruption of dendritic spines and synapses, which itself is a pivotal pathogenic step (Morfini et al., 2009; Wei et al., 2009; Wishart et al., 2006). In FTD, extensive synaptic loss and reduction in the number of spines have been documented in diseased cortex (Ferrer, 1999; Lipton et al., 2001). Given its role in endosomal trafficking and plasma membrane deformation, ESCRT-III might plausibly control aspects of synaptic biology. Here, we examine the possible impact of CHMP2B mutants and CHMP2B depletion on the development of dendritic spines. CHMP2B^{intron5} and CHMP2B^{Δ10} was expressed in hippocampal neurons without causing apparent anomalies in endosomal morphology, autophagosome amount or cell viability. The mutants potently suppressed the growth of spine heads, strongly lowering the proportion of mushroom spines. Very similar effects were obtained with an siRNA targeting endogenous CHMP2B, consistent with dominant-negative action of the mutants. Physiologically, CHMP2B^{Δ10} caused a drop in the frequency and amplitude of spontaneous excitatory synaptic currents, with selective disappearance of large currents. We propose that CHMP2B and potentially ESCRT-III are required for the maturation of dendritic spines, and that pathogenic CHMP2B mutants perturb this process. To the extent that maturation correlates with functional potentiation, these results implicate ESCRT-III in synaptic plasticity. In the protracted course of FTD, CHMP2B mutations might affect synaptic homeostasis and plasticity long before inducing massive neuronal death.

Results

Expression of CHMP2B variants in hippocampal neurons

To study the neuronal effects of CHMP2B proteins, hippocampal neurons were transfected at 10 days in vitro (DIV) with plasmids encoding N-terminally tagged CHMP2B^{wt} (wild type), CHMP2B^{intron5} or CHMP2B^{Δ10} (Fig. 1). Using immunofluorescent staining with anti-tag antibody, expression of these plasmids could be reliably detected up to 5 days after transfection. The subcellular distribution of the mutant proteins clearly differed from that of wild type (Fig. 1B; Fig. 2, left; Fig. 3, left). Wild-type CHMP2B was homogeneously distributed throughout the entire neuronal cytoplasm, including in axons, dendrites and dendritic spines (Fig. 1B, arrows). By contrast, both CHMP2B^{intron5} and CHMP2B^{Δ10} formed varying numbers of small bright puncta, which were found in the soma and proximal dendrites. Larger aggregates were occasionally observed in the soma. To determine whether expression of CHMP2B mutants perturbed autophagy in our system, we performed co-transfection experiments with LC3–GFP as an autophagosome marker. In a vast majority of neurons, expression of either CHMP2B^{Δ10} or CHMP2B^{intron5} failed to induce clustering of LC3–GFP (Fig. 2, b2, c2). In support of this, despite evaluation by two independent investigators, we could not detect any autophagy-associated drop in the diffuse pool of LC3–GFP. Thus, in the present setting, pathogenic CHMP2B mutants did not substantially enhance autophagosome accumulation. Furthermore, to determine whether the mutant CHMP2B puncta observed in transfected neurons were related to endosomes, transfected neurons were doubly stained with anti-tag antibody and antibodies raised against either the early endosomal marker EEA-1 (Fig. 3, a2–c2) or the late-endosomal–lysosomal protein LAMP-1 (Fig. 3, d2–f2). No colocalisation was observed with these markers. These data suggest that the CHMP2B aggregates that form under our transfection conditions are not associated with endosomes.

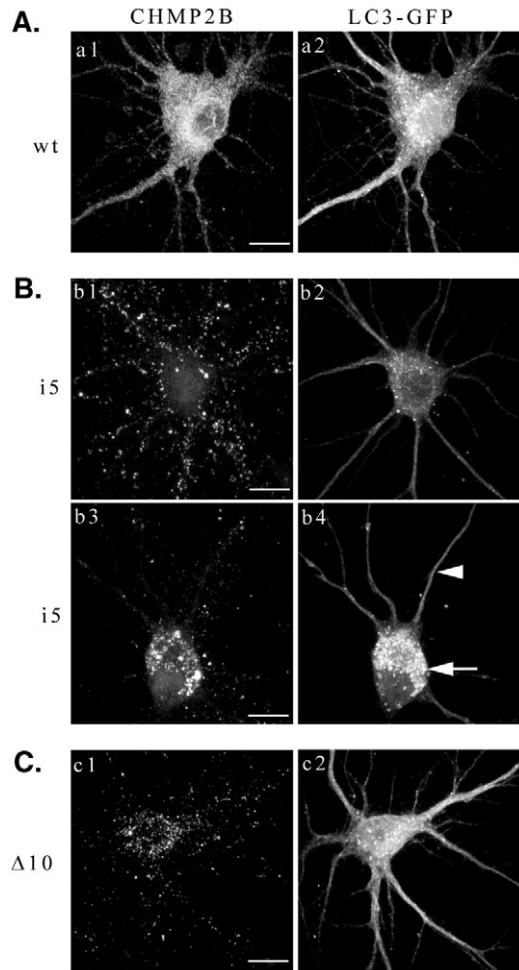


Fig. 2. Lack of LC3–GFP clustering in neurons expressing mutant CHMP2B. Neurons were co-transfected at 10 DIV with the indicated CHMP2B plasmids (left), together with the autophagosomal marker LC3–GFP. The cells were fixed 5 days later and processed for immunofluorescence staining with anti-tag antibody and Alexa-Fluor-594-coupled secondary antibody. Confocal images were acquired in both the immunofluorescence and GFP channels. Diffuse LC3–GFP localisation predominated upon co-transfection with CHMP2B^{wt} (a1,a2), CHMP2B^{Δ10} (c1,c2) and in a large majority of cases with CHMP2B^{intron5} (b1,b2). Autophagosome accumulation was seen in rare cells transfected with CHMP2B^{intron5} (b3, b4, arrow). Arrowhead: no autophagosomes were detected in the dendrites. Scale bars: 10 μm.

To visualise the morphology of neurons that had been expressing mutant CHMP2B for several days, the cells were co-transfected with CHMP2B constructs and a plasmid encoding the fluorescent protein mCherry, allowing staining of the whole cytosol. At 5 days after transfection, 75–80% of neurons co-transfected with empty vector, CHMP2B^{wt} or CHMP2B^{Δ10}, and 55% of neurons co-transfected with CHMP2B^{intron5} were healthy, as judged from the overall integrity of their neurites and the absence of neuritic swellings (supplementary material Fig. S1). These percentages did not change much after 10 days, and were largely sufficient to allow meaningful analysis of dendritic arbors and spines. Only healthy neurons were retained for further analysis.

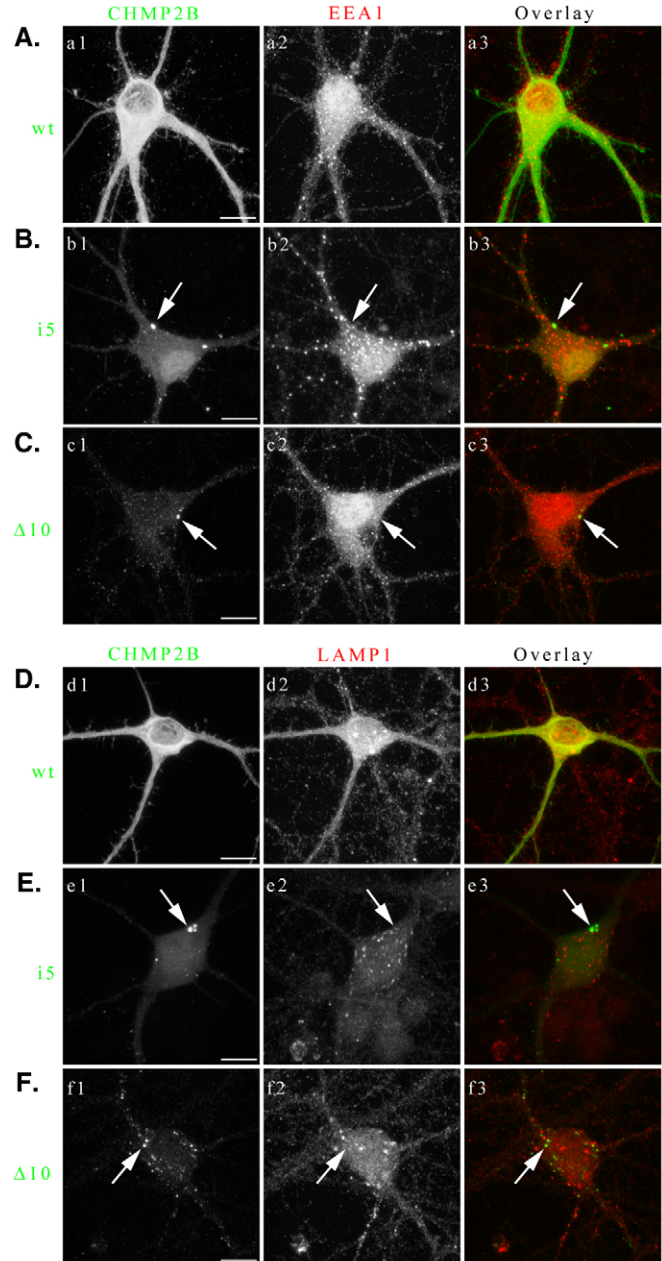


Fig. 3. Non-endosomal localisation of exogenously expressed CHMP2B proteins in hippocampal neurons. Neurons were doubly stained with monoclonal anti-tag antibody (a1–f1) together with polyclonal antibody against the respective marker (a2–f2), as indicated. Immunofluorescence was recorded by dual-channel confocal microscopy. Arrows indicate CHMP2B puncta. Note that they do not coincide with EEA1 (a2–c2) or LAMP1 (d2–f2) puncta. Scale bars: 10 μm.

The effect of CHMP2B constructs on dendritic arborisation was determined by Sholl analysis of neuronal morphology. For this, we measured the rate of increase in total neuritic length as a function of radial distance from the cell body (supplementary material Fig. S2). CHMP2B^{wt} and CHMP2B^{Δ10} had no significant effect on arborisation. CHMP2B^{intron5} induced a moderate (25%) decrease in average branching rate, but did not induce the large-scale retraction of dendrites that accompanies lethal perturbations of ESCRT-III (Lee et al., 2007).

CHMP2B mutants affect dendritic spine density and morphology

The dendritic morphology of neurons that were co-transfected with mCherry and CHMP2B plasmids was examined in detail by three-dimensional (3D) confocal imaging of mCherry fluorescence. Fig. 4A (a–d) shows representative views of neurons transfected with the different CHMP2B constructs. Stacks of serial optical sections were produced for each neuron and the NeuronStudio software package (Rodríguez et al., 2008; Rodríguez et al., 2006) was then used to generate 3D reconstructions of dendritic arbors and spines, and to count, measure and classify spines (see Materials and Methods). Fig. 4B shows a reconstructed dendritic segment obtained from a typical control neuron, and the results of automated identification of spine types. The volumes of the reconstructed spines followed a statistical distribution that closely resembled that described in a recent study of hippocampal spine dynamics (Yasumatsu et al., 2008) (supplementary material Fig. S3). Furthermore, the peak of our distribution (between 0.050 and 0.075 μm^3) was in the same range as published values ($0.058 \pm 0.034 \mu\text{m}^3$) previously obtained by electron microscopy for the spines of hippocampal neurons in dissociated culture at 14 DIV (Boyer et al., 1998). The distribution of spine lengths was also similar to previously published values (Fig. 4G). These data indicate that analysis by NeuronStudio correctly detected the spine population in our cultured neurons.

The density of spines (pooling all spine types) detected by this technique was determined for each neuron (Fig. 5A,B).

Overexpression of tagged, wild-type CHMP2B did not change the average density compared to control (co-transfection with empty vector). By contrast, expression of CHMP2B^{intron5} raised the average density of spines by 64% compared with control (Fig. 5A, column 3). However, many of these additional spines were very small (see below). These small spines were often hard to detect in uniformly thresholded 2D projections of image stacks, but were revealed by the 3D reconstruction procedure (supplementary material Fig. S4). Neurons expressing the CHMP2B ^{Δ 10} mutant also had a tendency to increase the density of their protrusions (average density 24% higher), but this trend did not reach significance (Fig. 5A, column 4).

To investigate the possible effect of CHMP2B mutants on spine dimensions, we determined the mean length of spines and the mean diameter of spine heads for each neuron. None of the CHMP2B constructs modified spine length (Fig. 5C,D). Wild-type CHMP2B did not change spine head diameter either. By contrast, mutant proteins strongly affected spine diameter. Expression of CHMP2B^{intron5} induced a 40% reduction in average spine diameter, whereas CHMP2B ^{Δ 10} reduced average diameter by 32% (Fig. 5E,F). These changes in average spine dimensions reflect the selective loss of large-headed spines. Fig. 5G,H shows the normalised distributions of spine lengths and spine head diameters in neurons transfected with each of the four plasmids. Both mutants had a clear, comparable effect on the distribution of spine diameters (Fig. 5H). In control neurons, thin spines (diameter $<0.2 \mu\text{m}$) predominated on top of a distinct population of larger spines,

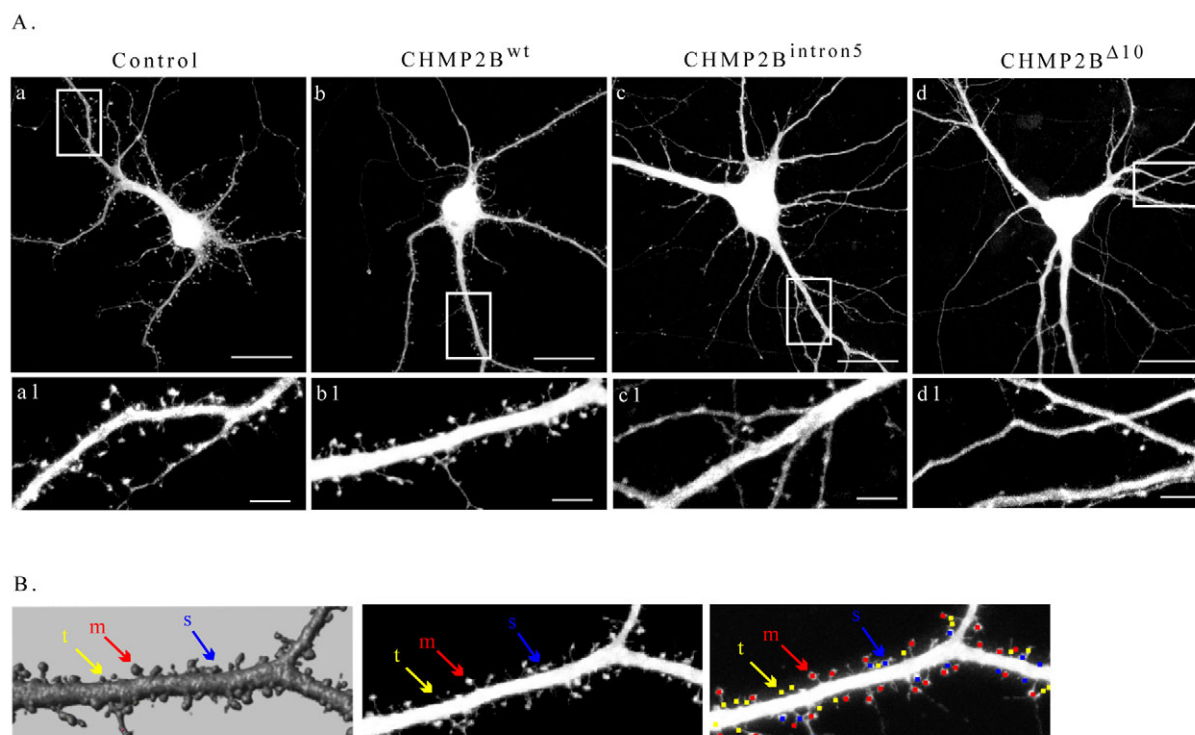


Fig. 4. Detection and classification of dendritic spines in transfected hippocampal neurons. (A) Neurons were co-transfected with the indicated constructs together with mCherry, fixed 5 days later and images of mCherry fluorescence were acquired by confocal microscopy. The figure shows maximal intensity projections of confocal image stacks. Control: empty pcDNA3 vector. The boxed regions in a–d (scale bar: 20 μm) were scanned at higher magnification in a1–d1 (scale bar: 5 μm). (B) Stacks of optical slices acquired in A served to generate 3D models of the dendrite, using the surface-defining Ray Burst algorithm implemented in NeuronStudio (Rodríguez et al., 2006). The dimensions of the modelled structures were automatically measured as described previously (Rodríguez et al., 2006) and used to identify and classify spines. Left: surface rendering of a segment from the dendrite shown in b1. Middle: maximal intensity projection of optical sections from the same segment. Right: automated spine detection and classification. Appropriately coloured dots are superimposed onto the spines. Yellow (t): thin spines; red (m): mushroom spines; blue (s): stubby spines.

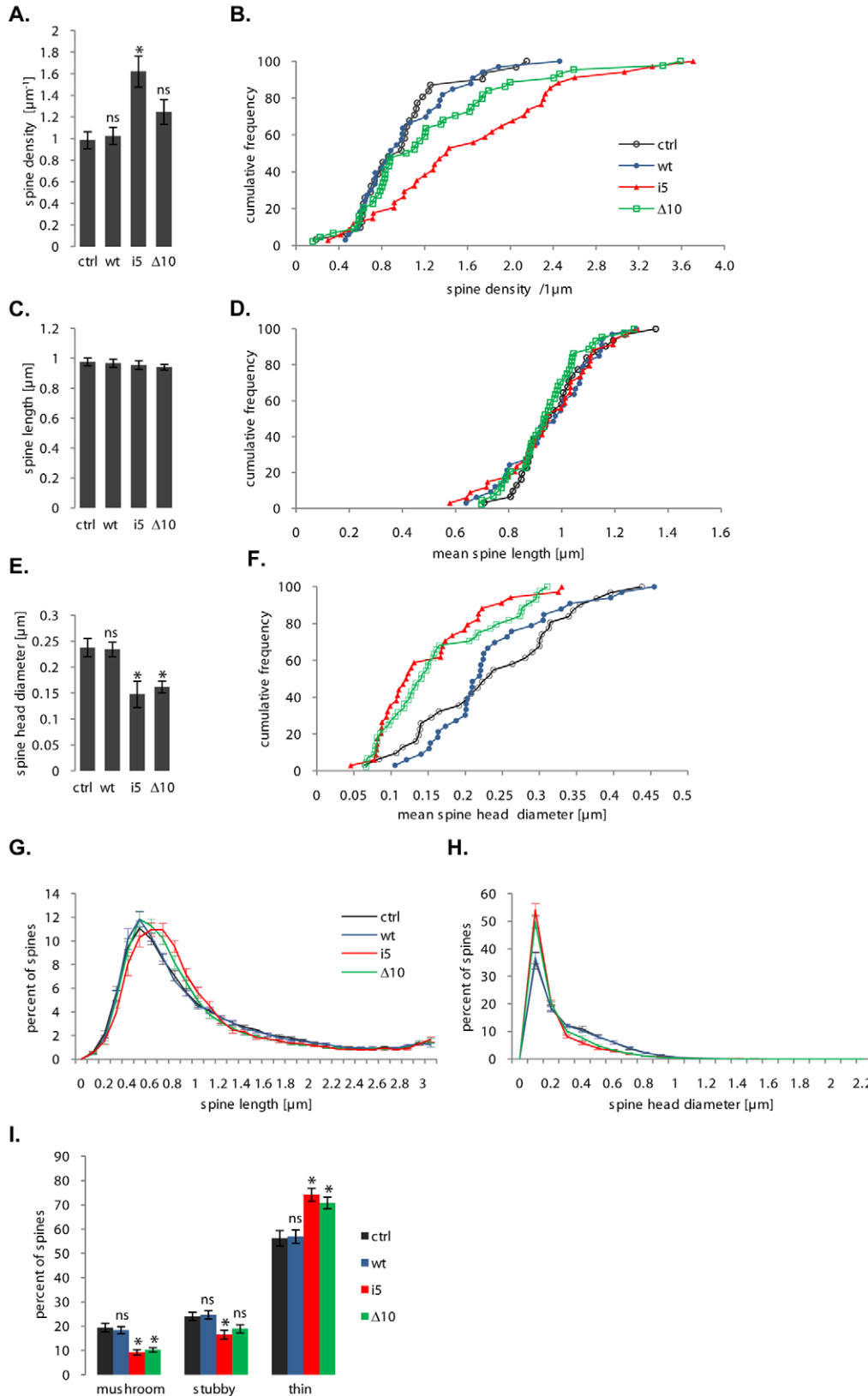


Fig. 5. Effects of FTD-linked CHMP2B mutants on the density and dimensions of spines. All parameters were measured on the same sets of neurons (pooled from three independent cultures). Ctrl, control plasmid ($n=31$ neurons); wt, tagged wild-type CHMP2B ($n=33$ neurons); i5, CHMP2B^{intron5} ($n=34$ neurons); $\Delta 10$, CHMP2B ^{$\Delta 10$} ($n=44$ neurons).

Measurements were obtained from 700–1500 μm dendrites and 600–1200 spines per neuron. (A) Mean spine counts per μm dendrite in neurons co-transfected with mCherry and the indicated plasmids. CHMP2B^{intron5} increases the total density of spines ($*P=0.0005$). The increase caused by CHMP2B ^{$\Delta 10$} remains non-significant (ns) with $P=0.09$.

(B) Cumulative frequency histogram of spine densities per neuron, corresponding to the dataset in A. (C) Mean length of spines per neuron. No significant difference was observed between conditions. (D) Cumulative frequency histogram of mean spine length per neuron, corresponding to dataset in C.

(E) Mean diameter of spine heads per neuron. Both mutants cause an overall shrinkage of spine heads ($*P=0.0005$ for both mutants). (F) Cumulative frequency histogram of mean spine head diameters per neuron, corresponding to the dataset in E. (G) Normalised distribution of spine lengths per neuron. Spine length histograms obtained for each neuron (0.1- μm -wide bins) were normalised to 100 total counts. The distribution shows the mean normalised values of each bin, for the respective neuron group. Error bars: s.e.m. for each bin. (H) Normalised distribution of spine head diameters per neuron. Spine diameter histograms obtained from each neuron were normalised and averaged as in F. Note the coincidence of the control and wild-type distributions, and that of the two mutant distributions. (I) Effects of FTD-linked CHMP2B mutants on the morphological type of spines. Histogram shows the mean percentages per neuron of spines with mushroom-like, stubby and thin morphologies. Both mutants potentially reduce the mushroom spine fraction ($*P<0.000001$ for both mutants).

CHMP2B^{intron5} also reduces the fraction of stubby spines ($*P=0.005$) but CHMP2B ^{$\Delta 10$} does not ($P=0.09$). Conversely, both mutants increase the thin spine fraction ($*P=0.0001$ for both mutants).

CHMP2B^{intron5} (IQR, 2.89 μm) or CHMP2B ^{$\Delta 10$} (IQR, 3.12 μm). Because spines with similar head width might differ in the size of their neck, with important consequences for their physiology (Noguchi et al., 2005), we determined how CHMP2B mutants

represented as a shoulder and tail in the distribution [interquartile range (IQR), 5.98 μm]. This subset of larger spines was still present in neurons transfected with CHMP2B^{wt} (IQR, 6.00 μm), but strongly reduced following transfection with either

CHMP2B^{intron5} (IQR, 2.89 μm) or CHMP2B ^{$\Delta 10$} (IQR, 3.12 μm). Because spines with similar head width might differ in the size of their neck, with important consequences for their physiology (Noguchi et al., 2005), we determined how CHMP2B mutants

affected the basic morphological categories of spines. Fig. 5I shows that neurons expressing either mutant had an abnormally low fraction of mushroom spines, identified by their head vs neck width ratio. The fraction of spines with mushroom morphology was decreased by ~50% with both CHMP2B^{intron5} and CHMP2B^{Δ10}, because they were replaced by an enlarged proportion of thin spines. Stubby spines were also reduced in number, but to a smaller extent, by expression of CHMP2B^{intron5}. The average diameter of spines in the mushroom spine subset (0.56 μm) did not significantly change in cells transfected with the mutants, confirming the consistency of morphotype identification.

Taken together, these data indicate that expression of a mutant ESCRT-III subunit linked to a human neurodegenerative disease can strongly affect the density and morphology of dendritic spines, and disrupt the normal pattern of spine development.

A CHMP2B mutant affects miniature excitatory synaptic currents

To determine whether the effects of mutant CHMP2B on spine morphology correlated with functional changes at synapses, we recorded excitatory synaptic currents from cultured hippocampal

neurons that had been co-transfected with GFP together with empty vector, or together with vectors encoding wild-type CHMP2B or CHMP2B^{Δ10}. Transfected cells were identified by GFP fluorescence. We monitored the frequency and amplitude of miniature excitatory postsynaptic currents (mEPSCs) as an indicator of possible effects of plasmids on synaptic strength. In total, 16 out of 18 transfected neurons were synaptically active; the two inactive neurons were discarded from analysis. Sample traces that were representative of each transfection condition are shown in Fig. 6A. A sequence of 128 consecutive mEPSCs was randomly picked from each recording, and the sequences were pooled according to the transfected plasmid. Mean inter-event intervals were calculated for each pool. Intervals were significantly longer between mEPSCs observed in neurons expressing CHMP2B^{Δ10} than in controls (Fig. 6B). Thus, the mean frequency of mEPSCs was lower in CHMP2B^{Δ10}-expressing cells than in control cells (1.47 vs 1.94 Hz), indicating a decrease in synaptic activity (Fig. 6B). The mean amplitude was slightly lower in mEPSCs of cells transfected with CHMP2B^{Δ10} than in those of control- or CHMP2B^{wt}-transfected neurons (12.6 vs 13.6 pA) (Fig. 6C). However, cumulative amplitude histograms indicated that CHMP2B^{Δ10} caused a

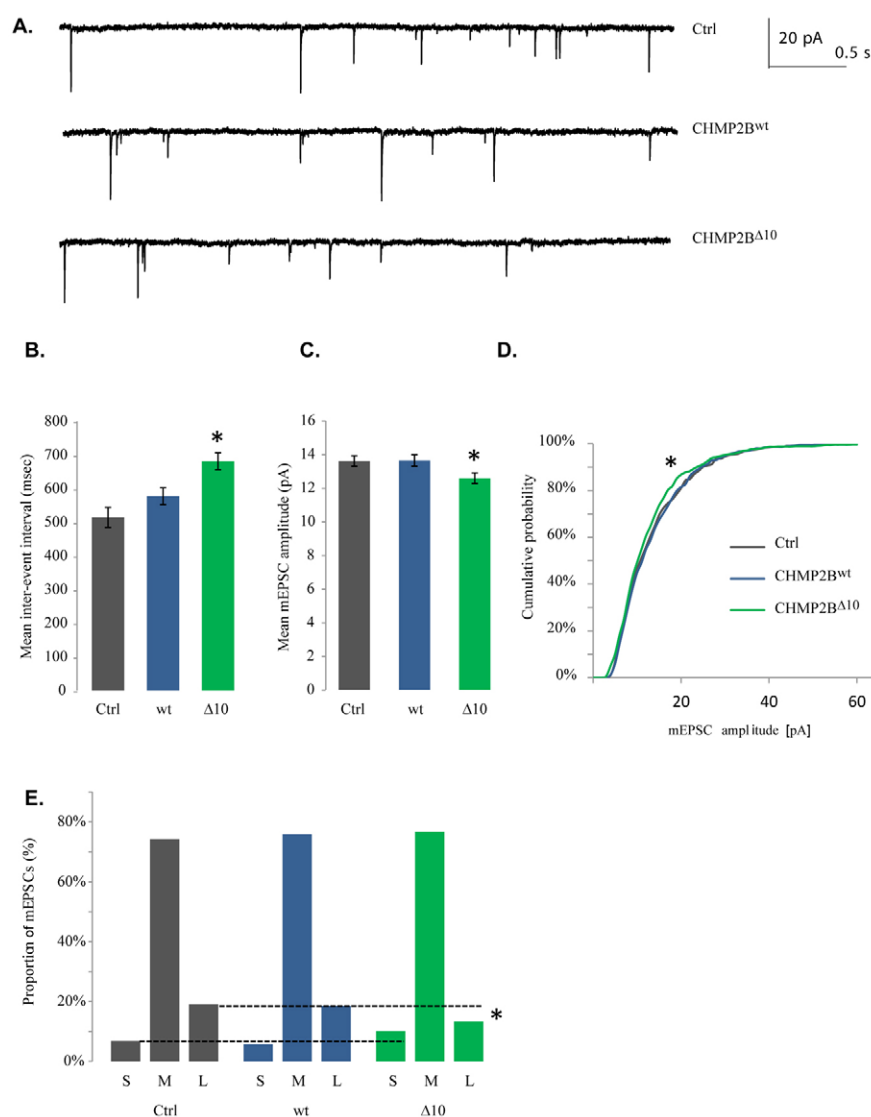


Fig. 6. Electrophysiological effects of wild-type and mutant CHMP2B.

mEPSCs were recorded from transfected neurons under voltage clamp in the whole-cell configuration, in the presence of tetrodotoxin and D-APV to isolate AMPA-receptor-mediated spontaneous synaptic currents (control: $n=4$ cells; CHMP2B^{wt}: $n=6$ cells; CHMP2B^{Δ10}: $n=6$ cells). (A) Representative sample traces from neurons co-transfected with GFP and control plasmid (top), CHMP2B^{wt} (middle) and CHMP2B^{Δ10} (bottom). (B) Mean duration of inter-event intervals along sequences of mEPSCs pooled from equivalently transfected neurons (control: $n=516$ events; CHMP2B^{wt}: $n=768$ events; CHMP2B^{Δ10}: $n=768$ events). Compared with control, intervals were significantly longer in mEPSCs from CHMP2B^{Δ10}-expressing neurons ($*P=0.00001$), but not from CHMP2B^{wt} neurons ($P=0.05$, significance threshold $\alpha=0.017$ with Bonferroni correction for multiple comparisons). (C) Mean amplitude of mEPSCs from the different transfection groups. The overall variation of mean amplitude as a function of transfected plasmid was significant (ANOVA: $F_{2,2049}=3.04$, $P=0.048$); the specific difference between the means of CHMP2B^{Δ10} and control was barely below threshold ($*P=0.026$ with Bonferroni-corrected $\alpha=0.025$). (D) Cumulative histogram of mEPSC amplitudes; same dataset as in C. * indicates significant reduction in the top quintile in the case of CHMP2B^{Δ10} (see Results and panel E). (E) Histogram of mEPSC amplitudes showing the specific reduction in the proportion of large currents (>20 pA) and the increase in small currents. S, <5 pA; M, $5 \leq i \leq 20$ pA; L, $i > 20$ pA. The two dashed lines refer to the respective proportions of large and small currents in the control neurons. The proportion of large currents was lower in neurons transfected with CHMP2B^{Δ10} compared with control or CHMP2B^{wt} neurons ($*P<0.05$).

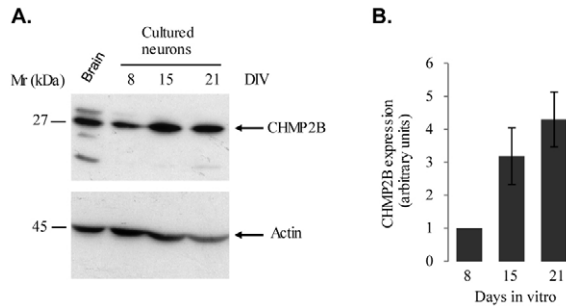


Fig. 7. Levels of endogenous CHMP2B increase during neuronal maturation in culture. Sister cultures of hippocampal neurons maintained in plastic dishes were lysed at the indicated time points (DIV). The lysates were analysed by SDS-polyacrylamide gel electrophoresis and western immunoblotting with anti-CHMP2B antibody. The blots were reprobed with anti-actin antibody to normalise for loading error. (A) Representative blot. Leftmost lane: rat brain lysate, showing the pattern of CHMP2B in vivo. (B) Films were scanned and the optical density of the CHMP2B band was measured in grey levels for each lane. Band intensities were normalised by dividing each value by the intensity of the actin band in the same lane. Care was taken to obtain immunodetection in the linear range. The graph shows mean normalised intensities at three time points ($n=3$ cultures). Error bars: s.e.m.

significant reduction in the frequency of large amplitude events, i.e. those belonging to the top quintile (Fig. 6D). mEPSCs with an amplitude larger than 20 pA (approximately twice the median amplitude), which represented up to 19% of mEPSCs in control neurons, were reduced by a third in neurons expressing CHMP2B^{Δ10}. Conversely, the proportion of small amplitude events (<5 pA) rose from 6.8% in controls to 10% in neurons expressing CHMP2B^{Δ10} (Fig. 6E). The drop in the frequency of large currents was not observed in neurons that overexpressed CHMP2B^{wt}. In view of the known correlation between spine head size and amplitude of AMPA-receptor-mediated synaptic currents (Matsuzaki et al., 2001), these data are consistent with the morphologically observed reduction in mushroom spines. Mutant CHMP2B might cause a reduction in the proportion of the more potent synapses and an increase in the proportion of weak synapses.

Endogenous CHMP2B is required for maturation of dendritic spines

Because dysregulated CHMP2B mutants affect spine morphogenesis, the issue arises of whether the endogenous normal protein plays some role in this process. Endogenous CHMP2B was clearly detectable in extracts from cultured neurons at 8 DIV and increased in older cultures, in which synaptogenesis and spine maturation are known to take place (Fig. 7). Immunofluorescent staining of the neurons with the anti-CHMP2B antibody showed the protein to be widely distributed throughout soma, axons and dendrites, similar to data obtained with the tagged wild-type protein (Fig. 8). To disrupt endogenous CHMP2B expression, we transfected cultured hippocampal neurons at 10 DIV with a pSuper-based plasmid vector encoding a previously described CHMP2B-specific shRNA (Lee et al., 2007). The efficiency of RNAi was ascertained by western blotting of transfected baby hamster kidney (BHK) cells (Fig. 8A). Transfected neurons could be tracked and outlined by mCherry, which was coexpressed from the same plasmid. Immunofluorescent staining with anti-CHMP2B antibody confirmed the efficient downregulation of endogenous CHMP2B

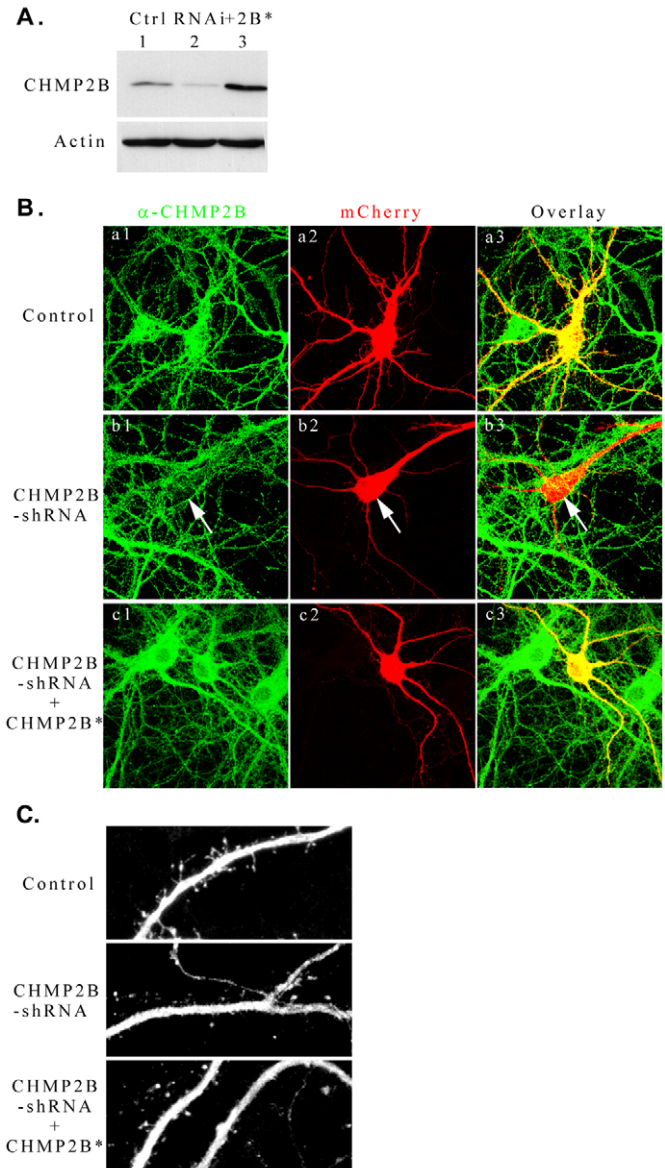


Fig. 8. Knockdown of endogenous CHMP2B in hippocampal neurons.

(A) To verify the efficacy of the shRNA-encoding plasmid, the indicated plasmids were transfected in rodent (BHK) cells and equal protein amounts of transfected cell lysates were analysed by western immunoblotting with anti-CHMP2B antibody, or with anti-actin as a control. Lane 1: empty pSuper-mCherry plasmid; lane 2: shRNA-expressing plasmid; lane 3: shRNA-expressing plasmid co-transfected with vector encoding CHMP2B* (native CHMP2B cDNA with silent mutations at the siRNA target site). Note that the CHMP2B protein remaining after transfection of the shRNA plasmid largely originates from non-transfected cells in the culture. (B) Neurons were transfected at 10 DIV with the plasmids indicated on the left, fixed at 15 DIV and stained with anti-CHMP2B antibody and Alexa-Fluor-488-labelled secondary antibody. Confocal images were acquired in both the Alexa-Fluor-488 and mCherry channels. Representative images of transfected neurons are displayed. Control: empty pSuper-mCherry vector. Note the drop in immunofluorescence in the shRNA-expressing neuron (arrow) compared with surrounding cells, and the decreased green vs red ratio (overlay) compared with control or rescued cells. (C) Maximal intensity projections of image stacks, showing representative dendritic segments visualised by mCherry fluorescence in neurons transfected with the indicated plasmids.

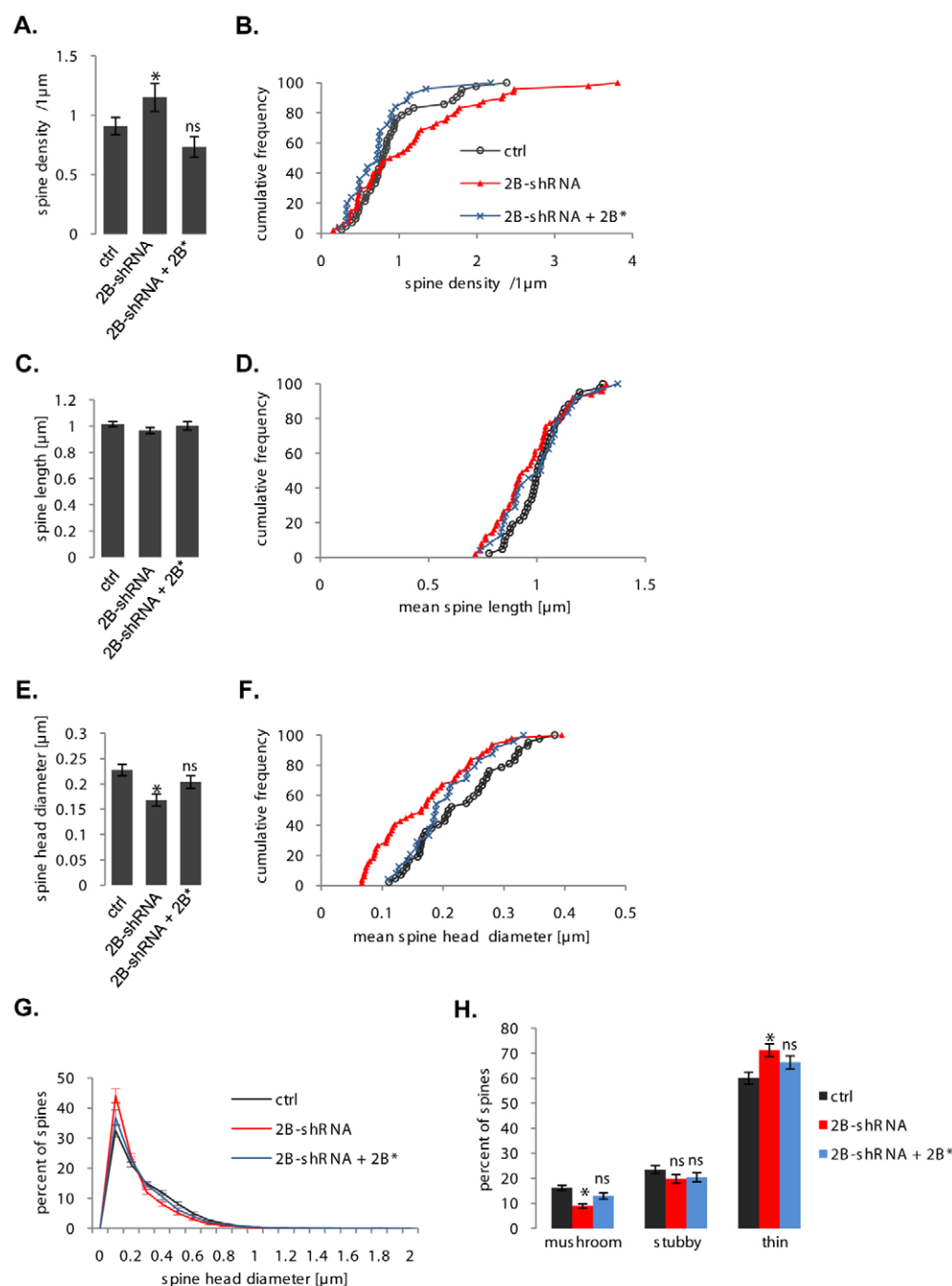


Fig. 9. Effects of CHMP2B depletion on the density and morphology of dendritic spines. All parameters were measured as in Figs 3 and 4. Ctrl: $n=42$ cells; shRNA: $n=48$ cells; shRNA together with rescuing CHMP2B: $n=25$ cells. (A) The mean density of spines varied as a function of CHMP2B depletion (ANOVA: $F_{2,112}=3.80$, $P=0.025$), although pairwise differences with control remained below significance ($*P=0.021$ vs rescued cells). (B) Cumulative frequency histogram of spine densities per neuron (normalised in percent); same data as in A. (C) CHMP2B depletion had no effect on the mean spine length per neuron. The CHMP2B shRNA induces a highly significant decrease ($*P<0.001$), which is rescued by re-expression of CHMP2B (ns, $P=0.19$). (D) Cumulative frequency histogram of spine lengths. (E) Mean spine head diameter per neuron. The CHMP2B shRNA induces a highly significant decrease ($*P<0.001$), which is rescued by re-expression of CHMP2B (ns, $P=0.19$). (F) Cumulative frequency histogram of spine head diameters. (G) Normalised distribution of spine head diameters. Note the superposition of 'control' and 'rescued' (2B-shRNA + 2B*) curves, and the recovery of larger spines in the 'rescued' profile. (H) Proportions of basic spine types. The CHMP2B shRNA potentially decreases the mushroom spine fraction ($*P<0.001$) and the effect is suppressed in the rescued cells (ns, $P=0.028$, corrected alpha=0.017).

expression in transfected neurons (Fig. 8B, middle panel). In agreement with published results (Lee et al., 2007), the CHMP2B shRNA did not affect neuronal viability. To verify the target specificity of RNAi, control experiments were performed in which CHMP2B shRNA was coexpressed with an RNAi-resistant CHMP2B mRNA (called CHMP2B*) (Fig. 8B, lower panel). Confocal imaging of mCherry and spine analysis were performed as in the case of mutant CHMP2B (Fig. 8C, Fig. 9).

Depletion of endogenous CHMP2B increased the average density of spines, and the increase was fully reversed upon rescue by CHMP2B* (Fig. 9A,B). CHMP2B depletion did not significantly affect the length of spines (Fig. 9C,D). By contrast, a highly significant reduction in mean spine diameter per neuron was observed in shRNA-transfected cells compared with controls; this

was rescued to a near-normal value upon coexpression of CHMP2B* (Fig. 9E,F). Similar to the case of neurons transfected with mutant CHMP2B, the size distribution of spine heads showed a loss of the large spine subset; this loss was largely reversed by rescue with RNAi-resistant CHMP2B (Fig. 9G). Spine classification revealed a 50% drop in the average proportion of mushroom spines, from 17% in control neurons to 9% in shRNA-transfected cells (Fig. 9H). This effect is equivalent to that observed upon expression of mutant CHMP2B. Upon coexpression of CHMP2B*, the average proportion of mushroom spines could be rescued to 13%, at which level the difference with control neurons was no longer significant (Fig. 9H). This demonstrates the specificity of the effects of CHMP2B shRNA. Taken together, these results indicate that CHMP2B is required for spine head expansion, a

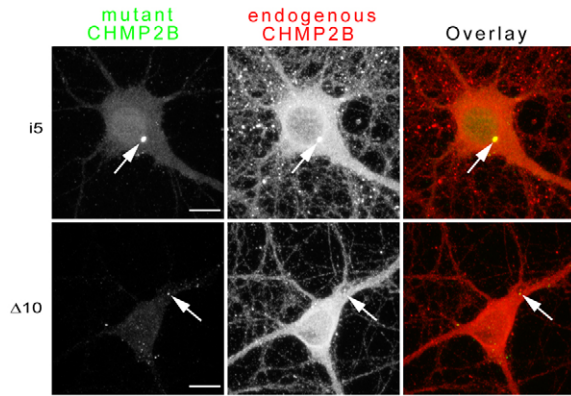


Fig. 10. Effect of mutant CHMP2B on the subcellular distribution of the normal protein. Hippocampal neurons were transfected with the indicated mutant, and processed for dual immunofluorescent staining with anti-tag and anti-endogenous-CHMP2B antibodies. Confocal images were acquired in both channels. Co-clustering of endogenous CHMP2B with mutant protein (arrows) was evident in some of the CHMP2B^{intron5} aggregates (upper panel), and faintly discernible in some of the CHMP2B^{Δ10} puncta (lower panel). Scale bars: 10 μ m.

basic structural aspect of synaptic plasticity. Furthermore, the data suggest that human-disease-linked CHMP2B mutants act as dominant negatives with respect to CHMP2B function in spine morphogenesis.

To determine whether mutant CHMP2B could perturb the subcellular distribution of the normal endogenous protein, neurons transfected with tagged CHMP2B^{intron5} or CHMP2B^{Δ10} were immunostained with both anti-CHMP2B and anti-tag antibodies (Fig. 10). For this, we took advantage of the fact that the anti-CHMP2B antibody was raised against the wild-type C-terminal region, and therefore does not recognise the mutant proteins. The larger CHMP2B^{intron5} aggregates recruited conspicuous amounts of the endogenous protein, inducing it to form abnormal clusters (Fig. 10, upper panel, arrow). Faint clusters of CHMP2B also occasionally overlapped with CHMP2B^{Δ10} puncta (Fig. 10, lower panel). However, the major, diffuse pool of endogenous CHMP2B remained unaffected. These results suggest that a fraction of native CHMP2B molecules might be perturbed in their biochemical function by interaction with mutant protein.

Discussion

Here we found that, in cultured hippocampal neurons, two FTD-linked CHMP2B mutants strongly perturbed the normal pattern of dendritic spine development. Both mutants caused a striking decrease in the proportion of large spines with mushroom morphology, i.e. those associated with potentiated synapses. This outcome was not associated with cell death. In keeping with these results, CHMP2B^{Δ10} induced a loss of large mEPSCs, namely those reflecting the activity of the strongest synapses. Consistent with the view that CHMP2B mutants act as dominant negatives, depletion of endogenous CHMP2B by RNAi resulted in changes that were very similar to those induced by mutant CHMP2B, and that could be largely suppressed by coexpression of rescuing protein. Together, these data show that normal spine morphogenesis requires CHMP2B, and that abnormal stoichiometry or pathological dysregulation of the protein can deeply affect the structure and function of spines.

Overexpression of CHMP2B^{intron5} in neurons has previously been shown to trigger a specific toxic process, leading to dramatic retraction of dendritic trees followed by cell death after 2–3 days; this lethality has been linked to excessive accumulation of autophagosomes (Lee et al., 2007; Lee and Gao, 2009). However, several lines of evidence indicate that the impairment in spine maturation described here occurs through a mechanism that is distinct from this toxic process. First, the changes in spine morphology were observed in healthy neurons. In particular, expression of CHMP2B^{Δ10} or knockdown of endogenous CHMP2B potentially affected spines, even though we found, in agreement with published data, that these perturbations of CHMP2B activity did not diminish neuronal viability. Second, alterations of spines did not correlate with changes in dendritic complexity. CHMP2B^{Δ10} elicited no detectable loss of dendritic branching and, in our conditions, CHMP2B^{intron5} only induced a 25% decrease in branching rate. This reduction remained modest compared with the 80% shortening of total dendritic length shown to occur in the early phase of CHMP2B^{intron5}-induced cell death (Lee et al., 2007). The CHMP2B shRNA caused a reduction in dendritic branching, but this might have been an off-target effect because, unlike the reduction in mushroom spines, it was not suppressed by coexpression of an RNAi-insensitive CHMP2B cDNA (A.B. and Y.G., data not shown). Third, when expressed in hippocampal neurons, neither of the CHMP2B mutants caused a clear-cut increase in LC3–GFP condensation onto autophagosomes. By contrast, a lethal degree of CHMP2B^{intron5} overexpression has been shown to induce strong clustering of LC3–GFP; furthermore, preventing autophagosome formation retarded the neuronal death caused by CHMP2B^{intron5} (Lee et al., 2007; Lee and Gao, 2009). Beyond some threshold level of expression, the ability of CHMP2B mutants to block the ESCRT-dependent fusion of autophagosomes to lysosomes (Filimonenko et al., 2007; Urwin et al., 2010) might favour the proliferation of toxic autophagosomes. The difference with our results might arise in part from the relatively low level of mutant CHMP2B expression we used in hippocampal neurons. Indeed, with fourfold higher amounts of CHMP2B^{intron5} plasmid, leading to higher expression, we observed toxicity similar to that described by Lee et al. (Lee et al., 2007) (although comparison is difficult, because Lee et al. did not mention the amounts of plasmid in their transfection assays). The non-endosomal location of mutant CHMP2B proteins in our experiments also seem at first sight to be at variance with previously published results from other cell types. However, HA-tagged CHMP2B^{intron5} did accumulate around endosomes when overexpressed in BHK cells (A. Belly, unpublished data). It should also be noted that, even in heterologous cells, a fraction of CHMP2B^{intron5} and CHMP2B^{Δ10} aggregates consistently fail to colocalise with endosomal markers (Skibinski et al., 2005) (A.B., unpublished). In transfected hippocampal neurons, presumably similar non-endosomal aggregates largely predominated. The occurrence of non-endosomal CHMP2B clusters is also consistent with the fact that, in vitro, activated ESCRT-III subunits can form large polymers in the absence of lipids (Lata et al., 2008). Our attempts to identify further components of the mutant CHMP2B clusters have so far been unsuccessful, except for the finding that endogenous CHMP2B is sometimes concentrated in CHMP2B^{intron5} granules. This suggests that native CHMP2B can be trapped in polymeric structures together with the mutant. Because much of the endogenous CHMP2B seemed to remain outside of the mutant CHMP2B puncta, sequestering of the native protein in the aggregates is unlikely to explain the apparent

dominant-negative effect of the mutants, especially in the case of CHMP2B^{Δ10}. Mutant molecules might instead perturb or displace their native counterparts in supramolecular structures that cannot be detected by simple light microscopy.

The mechanism(s) through which mutant CHMP2B proteins and CHMP2B depletion affect the morphology of spines will require elucidation. Given the endosomal trafficking function of ESCRT-III, one possibility is that disabling CHMP2B interferes with the endocytic recycling of a membrane protein that is crucial for spine growth. Examples of such proteins include the EphB and TrkB receptor tyrosine kinases and the GluR2 subunit of AMPA receptors (Henkemeyer et al., 2003; Passafaro et al., 2003). Of note, perturbation of a neurotrophin receptor such as TrkB would have implications for both spine morphogenesis and long-term survival of specific neurons. Alternatively, spine growth might require direct deformation of the dendritic plasma membrane by CHMP2B-containing ESCRT-III filaments (Hanson et al., 2008; Sweeney et al., 2006), or coupling of the actin cytoskeleton to ESCRT-III (Sevrioukov et al., 2005; Vaccari et al., 2009). Identification of CHMP2B-binding dendritic proteins and observation of ESCRT-III dynamics in live neurons might shed light on these possibilities.

Looking for a functional correlate of the CHMP2B^{Δ10} effect, we found that this mutant significantly decreased the frequency of mEPSCs. This result indicates that CHMP2B^{Δ10} elicits a decrease in synaptic activity. Moreover, the mutant induced a significant drop (32%) in the proportion of large mEPSCs. The two observations are in keeping with the loss of mature postsynaptic spines. In view of the general correlation between spine size and synaptic potency (Matsuzaki et al., 2001), the change in synaptic properties is consonant with the reduction in the proportion of mushroom spines induced by CHMP2B^{Δ10}. This result raises the intriguing possibility that pathogenic CHMP2B mutants might directly prevent synaptic potentiation and/or weaken previously strong synapses, and thereby perturb the functional connectivity of neurons. Further experiments are required to determine the role of CHMP2B and the impact of CHMP2B mutants on activity-dependent changes of spine structure, such as the enlargement associated with long-term potentiation.

Although lethal perturbation of autophagy might explain the loss of cortical neurons at the symptomatic stage of FTD-3 (Lee and Gao, 2009; Urwin et al., 2010), the protracted course of the disease, the lack of toxicity displayed by disease-linked mutants such as CHMP2B^{Δ10} and the low level of mutant CHMP2B mRNA in patients' brains lead one to argue that CHMP2B mutants might initially have pathogenic effects other than dysfunctional autophagy leading to cell death. Our results suggest that, in FTD-3, as in Alzheimer's disease, the pathogenic proteins might perturb synaptic plasticity and microstructure, long before overt cell death. A synaptotoxic mechanism would be consistent with observations of synapse loss in FTD (Ferrer, 1999; Lipton et al., 2001), and the widespread abnormalities in spine density and morphology seen in diverse neurodegenerative diseases (Fiala et al., 2002; Wishart et al., 2006). Understanding how defects in the highly conserved CHMP2B protein specifically lead to cortical degeneration might shed light on fundamental mechanisms of normal and pathological neurobiology.

Materials and Methods

Plasmids and antibodies

The mCherry plasmid was a kind gift from Pascal Dournaud (INSERM, Paris, France). The LC3-GFP plasmid was a kind gift from Tamotsu Yoshimori (National Institute of Genetics, Mishima, Japan). The GFP plasmid was pEGFP-C1 (Clontech).

The wild-type human CHMP2B cDNA was cloned from HeLa cells by RT-PCR, in frame with an N-terminal dimeric HA tag, using the following primer pair: 5'-CTCTCGAGGCCACCATGTACCCATACGACGTCCAGACTACGCTT-ACCCATACGACGTCCAGACTACGCTGCGTCCCTCTTCAAGAAGAA-3' and 5'-TACTCGAGCTGCAGTCACTAATCTACTCTCTAAAGCCTTGAGT-3'. The CHMP2B^{intronic5} mutant cDNA was amplified from the same cDNA preparation, using an alternate rearward primer (5'-TACTCGAGTCACACCTTCCAGAAATTC-AAT-3'). The two cDNAs were subcloned in pcDNA3.1 between the *Xho*I sites. To obtain the CHMP2B^{Δ10} cDNA, the C-terminal part was first synthesised in vitro using megaprimers (5'-ATGCCAGGATATTGTGAATCAAGTCTTGATGAAATTG-GAATTGAAATTTCTGGAAAGGTGTTGCACCACTTCTAGAAGCTTACC-3' and 5'-TAATCTTGAATTGCCATTAGACGCTTCACTGTGATGTAGACGT-TGTAGTAAAGGTAAATGGTAAGCTTCTAGAAGTTGGTGCAAC-3') and then fused with the CHMP2B^{intronic5} cDNA. The cDNAs were subcloned in pcDNA3.1 between the *Eco*RV and *Not*I sites. The pSuper-mCherry plasmid was constructed by removing GFP from pSuper-Neo-GFP (Oligoengine) and replacing it with mCherry. The shRNA targeted the rat CHMP2B sequence at positions 578–596 (5'-GACACTACAACAATGCAG-3') according to Lee et al. (Lee et al., 2007) and the encoding oligonucleotide was cloned between the *Hind*III and *Bgl*II sites of pSuper-mCherry. The RNAi resistant CHMP2B cDNA was generated by introducing four silent mutations in the target sequence (yielding 5'-GACGTTACAGACGATGCAA-3') by means of the QuikChange mutagenesis kit (Stratagene). All plasmids were verified by sequencing (Cogenics, Meylan, France), and initially tested in transfected BHK cells by immunoblotting and immunofluorescence with anti-tag antibody. The following polyclonal antibodies were purchased from Abcam (Cambridge, UK): anti-CHMP2B, anti-EEA1, anti-LAMP1. Anti-HA-tag antibody was from Cell Signaling Technology (Beverly, MA), anti-myc-tag antibody from Santa Cruz (CA) and anti-actin antibody from Chemicon.

Neuronal culture and transfection

Primary cultures of hippocampal neurons were prepared according to a modification of the procedure described previously (Banker and Goslin, 1998). Handling and sacrifice of animals were in conformity with European law (EEC Directive no. 86/609) and the internal regulations of INSERM. Hippocampi were dissected out from embryonic day 19 (E19) rat embryos, digested with trypsin and hippocampal cells were seeded at a density of 12,000 per cm² onto acid-washed glass coverslips (13 mm diameter, Marienfeld, Germany) that had been precoated with 50 µg/ml poly-D-lysine (Sigma). Cultures were maintained in serum-free Neurobasal medium containing 2 mM glutamine, 1 mM sodium pyruvate, 10 µg/ml penicillin and streptomycin and 2% B27 supplement (Invitrogen). For transfection, all plasmids were purified using the Endotoxin-free purification kit (Qiagen, Hilden, Germany). Preliminary experiments established that CHMP2B^{intronic5} toxicity was minimal when transfected at the dose used here. The conditioned culture medium was removed and saved, and coverslips were placed in 2 ml minimal essential medium (MEM; Invitrogen) containing 2 mM glutamine, 1 mM sodium pyruvate, 15 mM HEPES, NaOH (pH 7.35). 0.5 µg CHMP2B plasmid (or control vector) was mixed with 2.5 µg mCherry, GFP or LC3-GFP plasmid, diluted into 250 µl transfection medium and combined with 1.5 µl of 'Plus' reagent and then 4 µl Lipofectamine LTX (Invitrogen). The mixture was incubated for 25 minutes at room temperature (RT), then added to the dishes, which were left to incubate at 37°C for 1 hour. The transfection solution was removed and the conditioned medium was returned to the dishes. A total of 20–60 neurons per coverslip were usually transfected.

Fixation and immunostaining

The coverslips were rinsed in PBS and incubated for 8 minutes in PBS containing freshly prepared 4% p-formaldehyde and 4% sucrose at RT. After 3–4 washes in PBS, the cells were permeabilised by incubating in PBS containing 0.3% Triton X-100 for 10 minutes at RT. After washing, coverslips were pre-incubated in blocking solution [PBS containing 2% goat preimmune serum and 1% bovine serum albumin (Sigma-Aldrich)] for 1 hour, then in blocking solution containing 0.5–1 µg/ml primary antibody (or antibody mixture) at RT. After washing, incubation with secondary antibody conjugated to Alexa Fluor 488 or Alexa Fluor 594 (Molecular Probes, 0.2 µg/ml) and final washes, coverslips were gently dried and mounted on slides in Mowiol medium. The specificity of immunofluorescence was routinely verified by staining control cultures that had been transfected with empty pcDNA vector (for anti-tag antibodies) or by omitting the primary antibody in control incubations. The specificity of anti-CHMP2B antibody was further confirmed by RNAi-mediated extinction of immunofluorescence.

Microscopy

Images of fluorescent neurons were acquired with a Leica SP-E laser scanning confocal microscope equipped with a 100× Leica Neofluar objective with NA 1.3. Laser power was adjusted to maximise the dynamic range of each sample. For dual-colour samples, the adjustable spectral window of fluorescence collection was set for each channel with a singly coloured control sample, so that cross-contamination between channels was avoided. Stacks of 0.2-µm-spaced optical sections were acquired (averaging over four scans per pixel, 512×512 pixels) with the required electronic magnification. For spine analysis, any neuron showing signs of neuritic swellings or retraction was excluded. Dendritic segments located at approximately

equivalent distances from the soma were selected, and each of those was scanned at $1.5\times$ electronic zoom.

Image analysis

Image files were processed with MetaMorph (Molecular Imaging). All figures show maximal intensity projections. For analysis of spines, serial image files corresponding to z -stacks of 20–30 optical sections per dendritic segment were directly processed with NeuronStudio, a software package specifically designed for spine detection and analysis (Rodriguez et al., 2008; Rodriguez et al., 2006) (<http://www.mssm.edu/cnic/tools.html>). Voxel size was $0.143\times 0.143\times 0.200\text{ }\mu\text{m}$. The fluorescence threshold for inclusion in objects was dynamically set for each local sampling of the dendrite surface by the Isodata segmentation algorithm implemented in NeuronStudio. The seed location for automatic dendrite tracing was typically set near the base of a major proximal dendrite. At bifurcation points, the attach ratio was 1.5 and neurites shorter than $5\text{ }\mu\text{m}$ were not retained. After modelling of the dendrite surface, protrusions with a minimum volume of 5 voxels ($0.020\text{ }\mu\text{m}^3$), length of between $0.2\text{ }\mu\text{m}$ and $3\text{ }\mu\text{m}$ and a maximal width of $3\text{ }\mu\text{m}$ were retained as spines. Following default settings of the program and the empirical classification rule defined by Rodriguez et al. (Rodriguez et al., 2008), spines with a minimum head diameter of $0.35\text{ }\mu\text{m}$ and minimum head vs neck ratio of 1.1 were classified as mushroom spines. Non-mushroom spines with minimum volume of 10 voxels ($0.040\text{ }\mu\text{m}^3$) were classified as stubby spines. All other spines were considered thin. The typical percentages of the three spine types that we obtained were close to those found by Rodriguez et al. (Rodriguez et al., 2008). Measurements obtained by NeuronStudio were transferred to a spreadsheet (Excel or Gnumeric) for analysis. Sholl analysis was also performed with NeuronStudio, using single-plane lower magnification views centred on the cell soma. For each neuron, a series of $2\text{-}\mu\text{m}$ -spaced concentric circles centred on the soma were drawn as reference marks, starting with a circle just large enough to enclose the cell body. The total length of neurites within two consecutive circles was measured, and the measurement was repeated for increasingly large circle radii. Stepwise increases in neuritic length were plotted as a function of radial distance from the soma.

Cell degeneration assay

Neurons were transfected with $0.5\text{ }\mu\text{g}$ CHMP2B plasmid and $2.5\text{ }\mu\text{g}$ mCherry as above. After fixation and mounting onto slides, neurons were observed under an epifluorescence microscope (Zeiss Axiovert 200M) with a $63\times$ objective (1.3 NA) and a Rhodamine filter, and scored as dead or alive according to morphological criteria (see Results). The actual presence of coexpressed CHMP2B was verified by immunofluorescent staining with anti-tag antibody, using the GFP filter.

Electrophysiology

Spontaneous tetrodotoxin-resistant mEPSCs were recorded by means of the whole-cell configuration of the patch clamp method (Hamill et al., 1981). The recording medium contained (in mM): 136 NaCl, 5 KCl, 2 CaCl_2 , 1 MgCl_2 , 10 HEPES, 10 glucose, 0.0005 TTX, 0.025 D-APV, pH 7.4 (NaOH). Patch pipettes were made with the DMZ Universal Pipette puller (Zeitz Instruments, Germany) from thick wall borosilicate glass capillaries (1.5 mm outside diameter $\times 0.86\text{ mm}$ internal diameter) (Clark Electromedical Instruments, Phymep, France). Filled with a medium consisting of (in mM): 130 Cs-gluconate, 5 EGTA, 1 MgCl_2 , HEPES, 4 $\text{Na}_2\text{-ATP}$, pH 7.2 (CsOH), they had a resistance of 3–4 M Ω . Glass coverslips were put on the stage of an upright Olympus microscope (BX51WI, Olympus, France) equipped with a water immersion objective lens ($20\times$, N.A. 0.95, Olympus, France). GFP-expressing cells were voltage clamped at a holding potential of -70 mV and the mEPSCs were recorded and then analyzed off-line by means of the pClamp software (Molecular Devices, Dipsi, France). Synaptic currents, filtered at 1 kHz , were sampled at 10 kHz on an Axoclamp 200B amplifier (Molecular Devices, Dipsi, France). The experiments were conducted at RT ($20\text{--}22^\circ\text{C}$).

Western immunoblotting

Neurons were plated in plating medium at a density of 24,000 cells per cm^2 onto 35 mm plastic dishes (Nunc) that had been pre-coated with $50\text{ }\mu\text{g/ml}$ poly-D-lysine, and grown as described for coverslips. Sister dishes were withdrawn at the indicated time points and cells were lysed in lysis buffer containing 1% Triton X-100, 0.2% SDS, 10 mM NaF, 10 mM β -glycerophosphate (pH 7.5) and protease inhibitor mixture (Complete, Roche Molecular), and frozen. All lysates from a given culture were loaded on the same 10% SDS-polyacrylamide gel ($10\text{ }\mu\text{g}$ total protein per lane) and analysed by electrophoresis and immunoblotting with anti-CHMP2B antibody and anti-actin antibody. Bands were revealed by chemiluminescence (Pierce Femto reagent). Luminographs were scanned (300 dpi, 8-bit scale) and the resulting image files were analysed with MetaMorph. Grey levels measured for CHMP2B bands were normalised to the corresponding actin bands.

Statistical analysis

The statistical significance of overall variations within sets of conditions was determined by one-way ANOVA. The significance of pair-wise differences between conditions was then assessed by post-hoc one-tailed t -tests using the Bonferroni method. Unless indicated otherwise, all the reported P values refer to the difference with the control condition. We verified that criteria for robust ANOVA were satisfied;

moreover, Kruskal-Wallis analysis of mean rank variance yielded the same qualitative results as ANOVA. For analysis of mEPSC frequency, the significance of the transfection effect was confirmed by two-way ANOVA on a balanced subset of mEPSCs, separating the effect of plasmid identity from intrinsic neuron-to-neuron variation owing to the variability of innervation in the culture. The significance of differences between multiple frequency distributions was assessed with the χ^2 test. A post-hoc test of pairwise differences used the Marascuilo procedure (NIST Handbook of statistics, <http://www.itl.nist.gov/div898/handbook/>). For Sholl analysis, curves were compared by two-way ANOVA, separating the effect of plasmid identity from that of radial distance. Post-hoc comparisons between curves were performed by the Bonferroni method. All calculations were performed with the statistics-oriented spreadsheet Gnumeric (<http://projects.gnome.org/gnumeric/>) or with OpenStat (<http://statpages.org/miller/openstat/>). All error bars show s.e.m.

A. Belly was supported by the Fondation France Alzheimer. G.B. was supported by the Ministère de l'Enseignement Supérieur et de la Recherche. Work was funded by INSERM, Université Joseph Fourier and Fondation France Alzheimer. We thank David Béal for technical assistance, Anne Petiot for advice on autophagy assays, Douglas Ehlenberger for help with NeuronStudio, Tamotsu Yoshimori for the gift of LC3-GFP, Pascal Dournaud for the gift of mCherry, Winfried Weissenhorn for discussions, Jeremy H. Henley for critical reading of the manuscript, two anonymous reviewers for suggestions and all members of the lab for support.

Supplementary material available online at

<http://jcs.biologists.org/cgi/content/full/123/17/2943/DC1>

References

- Bajorek, M., Schubert, H. L., McCullough, J., Langelier, C., Eckert, D. M., Stubblefield, W. M., Uter, N. T., Myskza, D. G., Hill, C. P. and Sundquist, W. I. (2009). Structural basis for ESCRT-III protein autoinhibition. *Nat. Struct. Mol. Biol.* **16**, 754–762.
- Banker, G. and Goslin, K. (1998). *Culturing Nerve Cells*, 2nd edn. MIT Press.
- Boyer, C., Schikorski, T. and Stevens, C. F. (1998). Comparison of hippocampal dendritic spines in culture and in brain. *J. Neurosci.* **18**, 5294–5300.
- Carlton, J. G. and Martin-Serrano, J. (2007). Parallels between cytokinesis and retroviral budding: a role for the ESCRT machinery. *Science* **316**, 1908–1912.
- Fabrikant, G., Lata, S., Riches, J. D., Briggs, J. A. G., Weissenhorn, W. and Kozlov, M. M. (2009). Computational model of membrane fission catalyzed by ESCRT-III. *PLoS Comput. Biol.* **5**, e1000575.
- Ferrer, I. (1999). Neurons and their dendrites in frontotemporal dementia. *Dement. Geriatr. Cogn. Disord.* **10**, 55–60.
- Fiala, J. C., Spacek, J. and Harris, K. M. (2002). Dendritic spine pathology: cause or consequence of neurological disorders? *Brain Res. Brain Res. Rev.* **39**, 29–54.
- Filimonenko, M., Stuffers, S., Raiborg, C., Yamamoto, A., Malerod, L., Fisher, E. M., Isaacs, A., Brech, A., Stenmark, H. and Simonsen, A. (2007). Functional multivesicular bodies are required for autophagic clearance of protein aggregates associated with neurodegenerative disease. *J. Cell Biol.* **179**, 485–500.
- Hamill, O. P., Marty, A., Neher, E., Sakmann, B. and Sigworth, F. J. (1981). Improved patch-clamp techniques for high-resolution current recording from cells and cell-free membrane patches. *Pflügers Arch.* **391**, 85–100.
- Hanson, P. I., Roth, R., Lin, Y. and Heuser, J. E. (2008). Plasma membrane deformation by circular arrays of ESCRT-III protein filaments. *J. Cell Biol.* **180**, 389–402.
- Henkemeyer, M., Itkis, O. S., Ngo, M., Hickmott, P. W. and Ethell, I. M. (2003). Multiple EphB receptor tyrosine kinases shape dendritic spines in the hippocampus. *J. Cell Biol.* **163**, 1313–1326.
- Hurley, J. H. and Emr, S. D. (2006). The ESCRT complexes: structure and mechanism of a membrane-trafficking network. *Annu. Rev. Biophys. Biomol. Struct.* **35**, 277–298.
- Lata, S., Schoehn, G., Jain, A., Pires, R., Piehler, J., Gottlinger, H. G. and Weissenhorn, W. (2008). Helical structures of ESCRT-III are disassembled by VPS4. *Science* **321**, 1354–1357.
- Lee, J. A. and Gao, F. B. (2009). Inhibition of autophagy induction delays neuronal cell loss caused by dysfunctional ESCRT-III in frontotemporal dementia. *J. Neurosci.* **29**, 8506–8511.
- Lee, J. A., Beigneux, A., Ahmad, S. T., Young, S. G. and Gao, F. B. (2007). ESCRT-III dysfunction causes autophagosome accumulation and neurodegeneration. *Curr. Biol.* **17**, 1561–1567.
- Lipton, A. M., Cullum, C. M., Satumtira, S., Sontag, E., Hynan, L. S., White, C. L., III and Bigio, E. H. (2001). Contribution of asymmetric synapse loss to lateralizing clinical deficits in frontotemporal dementias. *Arch. Neurol.* **58**, 1233–1239.
- Matsuzaki, M., Ellis-Davies, G. C., Nemoto, T., Miyashita, Y., Iino, M. and Kasai, H. (2001). Dendritic spine geometry is critical for AMPA receptor expression in hippocampal CA1 pyramidal neurons. *Nat. Neurosci.* **4**, 1086–1092.
- Morfini, G. A., Burns, M., Binder, L. L., Kanaan, N. M., LaPointe, N., Bosco, D. A., Brown, R. H., Jr, Brown, H., Tiwari, A., Hayward, L. et al. (2009). Axonal transport defects in neurodegenerative diseases. *J. Neurosci.* **29**, 12776–12786.
- Muziol, T., Pineda-Molina, E., Ravelli, R. B., Zamborlini, A., Usami, Y., Gottlinger, H. and Weissenhorn, W. (2006). Structural basis for budding by the ESCRT-III factor CHMP3. *Dev. Cell* **10**, 821–830.

- Noguchi, J., Matsuzaki, M., Ellis-Davies, G. C. and Kasai, H. (2005). Spine-neck geometry determines NMDA receptor-dependent Ca^{2+} signaling in dendrites. *Neuron* **46**, 609-622.
- Passafaro, M., Nakagawa, T., Sala, C. and Sheng, M. (2003). Induction of dendritic spines by an extracellular domain of AMPA receptor subunit GluR2. *Nature* **424**, 677-681.
- Rodriguez, A., Ehlenberger, D. B., Hof, P. R. and Wearne, S. L. (2006). Rayburst sampling, an algorithm for automated three-dimensional shape analysis from laser scanning microscopy images. *Nat. Protoc.* **1**, 2152-2161.
- Rodriguez, A., Ehlenberger, D. B., Dickstein, D. L., Hof, P. R. and Wearne, S. L. (2008). Automated three-dimensional detection and shape classification of dendritic spines from fluorescence microscopy images. *PLoS ONE* **3**, e1997.
- Rusten, T. E. and Simonsen, A. (2008). ESCRT functions in autophagy and associated disease. *Cell Cycle* **7**, 1166-1172.
- Saksena, S., Wahlman, J., Teis, D., Johnson, A. E. and Emr, S. D. (2009). Functional reconstitution of ESCRT-III assembly and disassembly. *Cell* **136**, 97-109.
- Sevrioukov, E. A., Moghrabi, N., Kuhn, M. and Kramer, H. (2005). A mutation in dVps28 reveals a link between a subunit of the endosomal sorting complex required for transport-I complex and the actin cytoskeleton in *Drosophila*. *Mol. Biol. Cell* **16**, 2301-2312.
- Skibinski, G., Parkinson, N. J., Brown, J. M., Chakrabarti, L., Lloyd, S. L., Hummerich, H., Nielsen, J. E., Hodges, J. R., Spillantini, M. G., Thusgaard, T. et al. (2005). Mutations in the endosomal ESCRTIII-complex subunit CHMP2B in frontotemporal dementia. *Nat. Genet.* **37**, 806-808.
- Slagsvold, T., Pattani, K., Malerød, L. and Stenmark, H. (2006). Endosomal and non-endosomal functions of ESCRT proteins. *Trends Cell Biol.* **16**, 317-326.
- Stuchell-Brereton, M. D., Skalicky, J. J., Kieffer, C., Karren, M. A., Ghaffarian, S. and Sundquist, W. I. (2007). ESCRT-III recognition by VPS4 ATPases. *Nature* **449**, 740-744.
- Sweeney, N. T., Brenman, J. E., Jan, Y. N. and Gao, F.-B. (2006). The coiled-coil protein shrub controls neuronal Morphogenesis in *Drosophila*. *Curr. Biol.* **16**, 1006-1011.
- Urwin, H., Authier, A., Nielsen, J. E., Metcalf, D., Powell, C., Froud, K., Malcolm, D. S., Holm, I., Johannsen, P., Brown, J. et al. (2010). Disruption of endocytic trafficking in frontotemporal dementia with CHMP2B mutations. *Hum. Mol. Genet.* **19**, 2228-2238.
- Vaccari, T., Rusten, T. E., Menut, L., Nezis, I. P., Brech, A., Stenmark, H. and Bilder, D. (2009). Comparative analysis of ESCRT-I, ESCRT-II and ESCRT-III function in *Drosophila* by efficient isolation of ESCRT mutants. *J. Cell Sci.* **122**, 2413-2423.
- von Schwedler, U. K., Stuchell, M., Müller, B., Ward, D. M., Chung, H.-Y., Morita, E., Wang, H. E., Davis, T., He, G.-P., Cimbora, D. M. et al. (2003). The protein network of HIV budding. *Cell* **114**, 701-713.
- Wei, W., Nguyen, L. N., Kessels, H. W., Hagiwara, H., Sisodia, S. and Malinow, R. (2009). Amyloid beta from axons and dendrites reduces local spine number and plasticity. *Nat. Neurosci.* **13**, 190-196.
- Wishart, T. M., Parson, S. H. and Gillingwater, T. H. (2006). Synaptic vulnerability in neurodegenerative disease. *J. Neuropathol. Exp. Neurol.* **65**, 733-739.
- Wollert, T. and Hurley, J. H. (2010). Molecular mechanism of multivesicular body biogenesis by ESCRT complexes. *Nature* **464**, 864-869.
- Wollert, T., Wunder, C., Lippincott-Schwartz, J. and Hurley, J. H. (2009). Membrane scission by the ESCRT-III complex. *Nature* **458**, 172-177.
- Yasumatsu, N., Matsuzaki, M., Miyazaki, T., Noguchi, J. and Kasai, H. (2008). Principles of long-term dynamics of dendritic spines. *J. Neurosci.* **28**, 13592-13608.
- Zamborlini, A., Usami, Y., Radoshitzky, S. R., Popova, E., Palu, G. and Gottlinger, H. (2006). Release of autoinhibition converts ESCRT-III components into potent inhibitors of HIV-1 budding. *Proc. Natl. Acad. Sci. USA* **103**, 19140-19145.